ADVANCED BIOSYSTEMS
www.adv-biosys.com

Osterix-mCherry Expression Allows for Early Bone Detection in a Calvarial Defect Model

*Sara E. Strecker, Shimon Unterman, Lyndon F. Charles, Dmitry Pivovarchick, Peter F. Maye, Elazer R. Edelman, and Natalie Artzi**

The process of new bone formation following trauma requires the temporal recruitment of cells to the site, including mesenchymal stem cells, preosteoblasts, and osteoblasts, the latter of which deposit minerals. Hence, bone repair, a process that is assessed by the extent of mineralization within the defect, can take months before it is possible to determine if a treatment is successful. Here, a fluorescently tagged Osterix, an early key gene in the bone formation cascade, is used as a predictive measure of bone formation. Using a calvarial defect model in mice, the ability to noninvasively track the Osterix transcription factor in an Osterix-mCherry mouse model is evaluated as a measure for bone formation following treatment with recombinant human Bone-Morphogenetic-Protein 2 (rhBMP-2). Two distinct delivery materials are utilized, an injectable nanocomposite hydrogel and a collagen sponge, that afford distinct release kinetics and it is found that cherry-fluorescent protein can be detected as early as 2 weeks following treatment. Osterix intensity correlates with subsequent bone formation and hence can serve as a rapid screening tool for osteogenic drugs or for the evaluation and optimization of delivery platforms.

1. Introduction

Recombinant human bone morphogenetic protein 2 (rhBMP-2) has been used extensively in the clinic to induce bone formation.[1–6] It is commonly used in lumbar spinal fusion, where a rhBMP-2-soaked collagen sponge is inserted between two vertebrae to encourage bone growth in the intervertebral space; it also has found applications in the repair of tissue defects and fractures.[5,7–9] This approach is not without challenges, however, due to the poorly targeted delivery of high-dose growth factor which can result in exuberant or ectopic bone formation and even an increased cancer risk.[10–12]

Extensive preclinical research has focused on developing novel biomaterials to better control the delivery of rhBMP-2 and further enhance bone formation in a safe manner. Some of these approaches focus on modifying the material to direct release, while others attempt to mimic the bone microenvironment in order to minimize the need for rhBMP-2.[13–18] Typically, outcomes for in vivo preclinical testing rely on measures of bone mineral deposition using X-ray or CT, which typically take at least 4 weeks to provide an early readout of efficacy, substantially hampering cycle time and costs during biomaterial iteration and optimization. More invasive and destructive techniques, such as histology, immunostaining, and gene expression analysis, can yield insights into earlier changes during the repair process, but are cumbersome and require sequential animal sacrifice. The costs, ethical concerns, and challenges in following longitudinal data without same-animal controls militate for the development of early noninvasive techniques to predict later bone mineralization of novel biomaterial designs for delivery of rhBMP-2.

Previous researchers have used single-photon emission computed tomography (SPECT) or positron emission tomography (PET) scans to obtain high-resolution spatiotemporal monitoring of early mineralization by tracking incorporation of labeled diphosphonate and fluoride into mineralizing tissues.[19–23] These techniques allow for high-resolution 2D imaging but are limited by the availability of specialized equipment, carry additional safety considerations, and require development of conjugated or radioactive reporters. Furthermore, these methods are limited to detecting low mineralization signals (by incorporation

S. E. Strecker, S. Unterman, L. F. Charles, E. R. Edelman, N. Artzi
Massachusetts Institute of Technology
Institute for Medical Engineering and Science
45 Carleton Street, E25-438, Cambridge, MA 02139, USA
E-mail: nartzi@mit.edu
D. Pivovarchick
Ort Braude College
51 Swallow Street, Karmiel, 2161002 Haifa, Israel
P. F. Maye
Department of Reconstructive Sciences
University of Connecticut
Farmington, CT 06032, USA
E. R. Edelman
Cardiovascular Division
Brigham and Women's Hospital
Harvard Medical School
Boston, MA 02115, USA
N. Artzi
Department of Medicine
Division of Engineering in Medicine
Brigham and Women's Hospital
Harvard Medical School
Boston, MA 02115, USA
The ORCID identification number(s) for the author(s) of this article can be found under https://doi.org/10.1002/adbi.201900184.

DOI: 10.1002/adbi.201900184

of a marker into the mineralizing tissue) but do not detect biological signals that precede mineralization and therefore make the differentiation of ectopic bone formation difficult.

The use of fluorescent mouse models in research has enabled noninvasive study of gene expression at a transcriptional level.[24,25] The Osterix-mCherry mouse model affords the visualization of Osterix through a red fluorescent protein (monomeric Cherry).[26] Osterix, a zinc finger transcription factor essential for early skeletal development and maintenance,[27–29] is crucial for bone formation,[30–32] and without it, a cartilaginous anlagen develops, but it does not mineralize.[33]

The Osterix-mCherry mouse was created using bacterial artificial chromosome (BAC) recombination-mediated genetic engineering (recombineering). A 40 kb region of a BAC containing the Osterix gene and its upstream promoter region was combined with a monomeric cherry fluorescent protein, allowing for skeletal specificity without the additional gene expression often seen with BAC mice.[11] By utilizing this skeletally specific fluorescent mouse model, early stages of osteogenesis can be elucidated by examining levels of cherry fluorescence.[34] We hypothesized that the Osterix mCherry mouse model combined with in vivo fluorescent imaging can be used as a screening tool for piloting new therapies for bone repair as mCherry expression is an indicator of early bone formation during normal skeletal development due to its linkage to the Osterix gene. Notably, the approach of using fluorescent reporters can be generalized to any specific biological signal that precedes a later functional output.

The goal of this approach is to allow for the rapid and cost-effective screening of biomaterial-mediated delivery of rhBMP-2. To evaluate the predictive power of this Osterix reporter on later mineralization, we directly compared the rhBMP-2-mediated repair of bilateral critical size calvarial defects in the mouse using two different biomaterial delivery systems. The first material was a collagen sponge in clinical use for the delivery of rhBMP-2. The second, a nanocomposite hydrogel, was recently developed to provide controlled delivery of drugs to orthopedic tissues and is designed to release rhBMP-2 at a slower rate than the largely uncontrolled collagen sponge. By studying differential rhBMP-2 release kinetics, Osterix expression, and bone mineralization over time, we demonstrate that we can monitor bone formation via fluorescence weeks before mineralization is evident on μCT. We also show that material design and drug release kinetics affect the levels of Osterix mCherry fluorescence and eventual bone formation, as evidenced by osteocalcin expression. This early view will allow us to track and to predict the kinetics of bone formation over time to reduce the cycle time needed when optimizing delivery systems for bone repair applications.

2. Results

2.1. Osterix-Cherry Mice Allow for Tracking of Pre-Osteoblastic/Mesenchymal Cells In Vivo

The Osterix-mCherry mouse shows bright red fluorescence during all stages of skeletal development, even before mineralization, with the intensity increasing during differentiation. This model allows for tracking the kinetics of skeletal development over time and visualizing the mesenchymal and osteocytic cellular infiltration into the defect space, as well as the eventual correlation between fluorescence and differentiation. In designing the Osterix-mCherry mouse model, the cherry reporter was placed upstream of the second translational start site of the Osterix gene in order to allow for the visualization of both isoforms of Osterix[35,36] (**Figure 1**A, red arrow). The founder lines were extensively characterized and showed high specificity toward skeletal elements as seen in a P2 mouse skull (Figure 1B) and cortical section from an adult mouse (Figure 1F). In the cortical section, there are three types of red-labeled cells; the osteocytes embedded within the bone, the osteoblasts on the bone surface, and putative mesenchymal cells within the bone marrow near the cortical surface (Figure 1F, blue arrows). These cell types are distinct and can be identified through morphology and location, though they have been extensively characterized in terms of gene and protein expression as well.[37–40]

The mesenchymal cells make up ≈2% of the nucleated cells within the marrow based on fluorescence activated cell sorting (FACS) sorting (Figure 1G). These cells can be FACS isolated and plated. They go on to form red fluorescent colonies by 24 h (Figure 1C). If osteogenesis is induced in culture, via adherence to the plastic of the culture dish, up to 80% of the cells gain red fluorescence as seen in the timeline (Figure 1D and Figure S1, Supporting Information) and areas with the brightest fluorescence correspond to areas of von Kossa staining within the culture at day 21 (Figure 1D,E), indicating that these cells are actively laying down mineral. Immunostaining for Osterix on tissue sections from the calvarial bone of adult mice show overlap between the immunostaining and the inherent fluorescent of the tissue (Figure 1H,I), indicating that this model is accurately identifying cells which are expressing Osterix based on red fluorescence.

2.2. Osterix-Cherry Expression Provides a Read-Out of Putative Bone Formation Before Mineralization, and Correlates with Neo-Osteogenesis

Bilateral 3.5 mm defects were created in the calvarium of Osterix-mCherry mice using a dental drill.[41] Care was taken to maintain the periosteum and avoid the central suture. rhBMP-2 (0.2 μg) and saline were each pipetted onto collagen sponges (the delivery vehicle for rhBMP-2-mediated spinal fusion in the clinic) which had been cut to fit into the defect space (**Figure 2**A,B). After closing, Osterix fluorescence was monitored weekly using IVIS Spectrum (In Vivo Imaging System, Perkin Elmer), and bone formation biweekly using μCT. Little to no mineralization appears at 2 weeks post-surgery (Figure 2E,F) for mice treated with rhBMP-2, while a robust Cherry signal is seen on IVIS at 2 weeks in the defect space (Figure 2C,D). To understand whether this indicates early neo-osteogenesis, tissue sections taken from rhBMP-2-treated Osterix-mCherry mice at 7 (Figure 2G), 28 (Figure 2H), and 56 days (Figure 2I) post-surgery were characterized based on location relative to the bone surface and organization within the defect space. Mesenchymal cells are located adjacent to the bone surface.

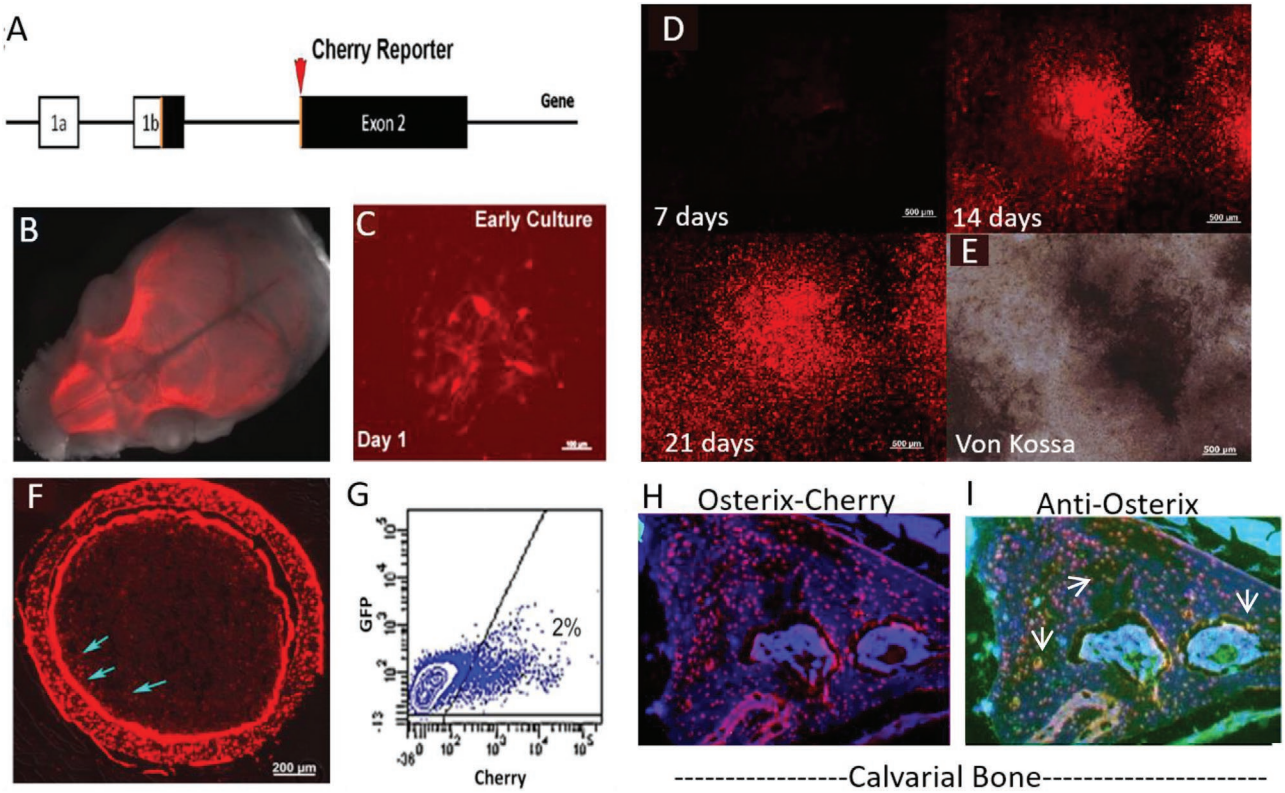

Figure 1. Osterix-Cherry mice allow for tracking of pre-osteoblastic/mesenchymal cells in vivo. A) Osterix-mCherry reporter construct showing the location of the fluorescent reporter in relation to the translational start site. B) Whole mount skull from P2 Osterix-mCherry reporter mouse indicating fluorescence is localized to skeletal tissue. C) Culture of bone marrow stromal cells (BMSC), showing colonies of mCherry cells after 24 h in vitro (scale bar = 50 µm). D) Time course of BMSC culture with consistent 15 ms exposure time confirming increasing brightness of colonies (scale bar = 500 µm). E) Mineralization by von Kossa at 21 days correlating with bright Osterix-mCherry expression (scale bar = 500 µm). F) Cortical section showing Osterix-mCherry expression within osteoblasts, osteocytes, and mesenchymal stem cells (blue arrows) (scale bar = 200 µm). G) Flow of freshly isolated bone marrow showing 2% of the cells are positive for mCherry expression. H) Calvarial section showing Osterix-mCherry expression within the bone. I) Same calvarial section seen in (H), immunostained for Osterix using a green secondary antibody, showing co-localization with (H) (white arrows, yellow cells).

Osteoblasts are located on the bone surface and in some cases appear brighter. Osteocytes are strongly cherry-positive cells embedded in the bone surface. Cherry-positive cells are infiltrating into the critical size defect, which is denoted with the dashed line. A strong periosteal response[2,42] is seen and cherry-positive mesenchymal cells (MSC) start to migrate from the edges of the defect toward the center as early as 1 week, post-treatment (Figure 2G). At 4 weeks, osteogenic cells start depositing new bone, and cherry-positive osteoblasts (OB) can be seen lining the newly formed bone surfaces, with mesenchymal stem cells (MSCs) still visible at 4 weeks. The onset of mineralization can be seen by 4 weeks on µCT (Figure 5E) and at 8 weeks, much of the remodeling has taken place and the defect is often filled. Fewer MSCs are visible, and much of the cherry-positive cells become osteoblasts on the bone surface and osteocytes (OC), which are embedded in the new bone.

2.3. The Effects of Differential Biomaterial-Mediated rhBMP-2 Release Profiles on Osterix Expression and Mineralization

Although early Osterix expression was clearly correlated with rhBMP-2 delivery and subsequent mineralization, it is not clear that this marker can distinguish between different rhBMP-2 release profiles and accurately predict the subsequent timing and degree of final mineralization. Calvarial defects were treated with rhBMP-2-loaded collagen sponges, as before, or a rhBMP-2-loaded nanocomposite (**Figure 3**A). This nanocomposite is a hydrolytically degradable, two-component tissue-adhesive hydrogel composed of an oxidized polysaccharide (dextran aldehyde) and a polyamine (poly(amido amine) dendrimer); it has been extensively studied with respect to its tissue adhesive properties, degradation properties, and drug release properties in the past.[43–45] The base hydrogel was further modified by the addition of phyllosilicate nanoplatelets of two different aspect ratios to reinforce the mechanical and rheological properties of the hydrogel, as previously reported.[46] The nanocomposite's compressive modulus was ≈200 kPa and the nanoplatelets adopted a well-distributed morphology in the material.[46] rhBMP-2 was loaded into the uncured macromer solution, which was then cured in situ in the calvarial defect; given the highly charged nature of the dendrimer and nanoplatelets, as well as the amine-reactive dextran macromers, it was expected that rhBMP-2 release would be substantially retarded in the nanocomposite compared to a collagen sponge.

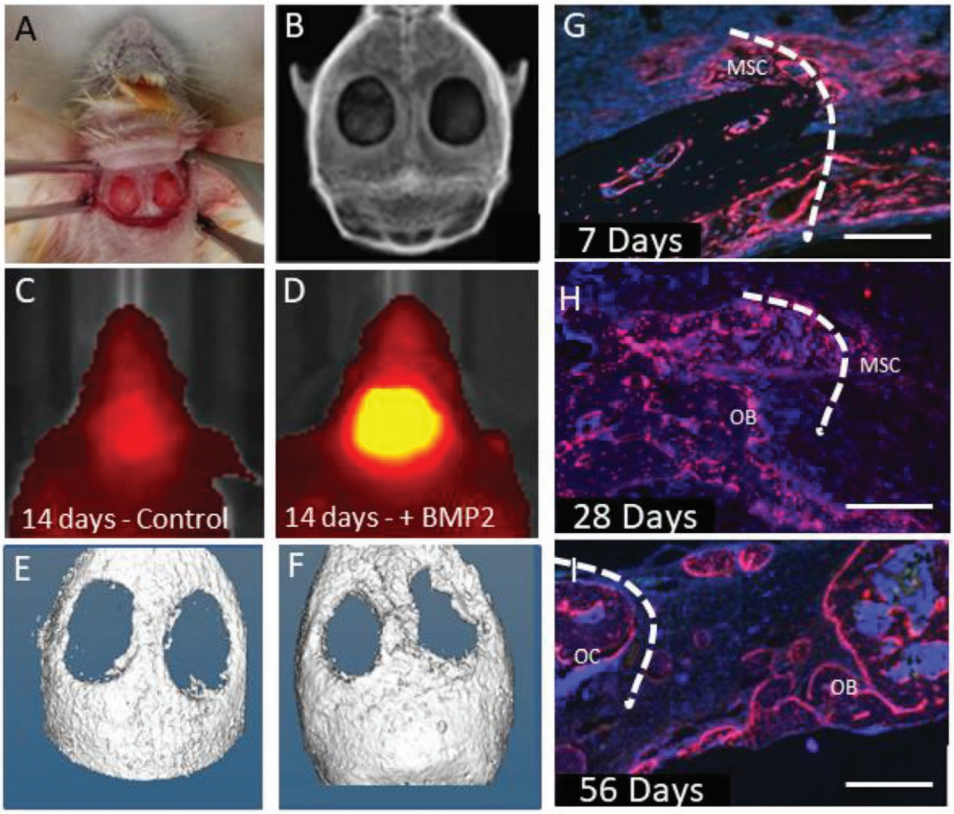

Figure 2. Osterix-Cherry expression provides a read out of putative bone formation before mineralization and correlating with neo-osteogenesis. A) Osterix mCherry mouse prepared for insertion of either collagen sponge or nanocomposite hydrogel. B) X-ray of bilateral calvarial defect post surgery. C) Osterix-mCherry mouse IVIS image 14 days post surgery with only collagen sponge inserted. E) Corresponding μCT image. D) Osterix-mCherry mouse IVIS image 14 days post surgery with collagen sponge infused with rhBMP-2. F) Corresponding μCT image. G) Calvarial defect treated with a collagen sponge infused with rhBMP-2 7 days post surgery showing mesenchymal stem cells (MSC) infiltrating the defect site (scale bar = 500 μm). H) Calvarial defect treated with a collagen sponge infused with rhBMP-2 28 days post surgery showing MSCs and Osterix-mCherry osteoblasts (OB) (scale bar = 500 μm). I) Calvarial defect treated with a collagen sponge infused with rhBMP2 56 days post surgery showing Osterix-mCherry osteoblasts (OB) and osteocytes (OC) (scale bar = 500 μm). Dotted line represents defect edge.

We hypothesized that the different release kinetics would affect either the timing or the extent of mineralization and that the level of Osterix expression would allow us to predict those differences. Release profiles of rhBMP-2 from each material were studied in vitro (Figure 3B). While the majority of rhBMP-2 was released from the collagen sponge within the first hour (87%), that same amount was released from the nanocomposites within 48 h, confirming that rhBMP-2 delivery from nanocomposite was slower than in the collagen sponge.

When implanted in a calvarial defect, empty material controls evidenced very low Osterix-mCherry fluorescence (measured by IVIS at 4 and 8 weeks, Figure 3D,G vs Figure 3P,S, respectively), and little to no mineralization (as quantified by μCT) (Figure 3E,H, vs Figure 3Q,T), while the rhBMP-2-loaded biomaterials induced a robust Osterix and mineralization response which can be seen on IVIS after 2 weeks and via μCT after 4 weeks.

To correlate μCT data on bone mineralization, we assessed collagen deposition at 4 and 8 weeks post-surgery and bone volume fraction (BV/TV) at 8 weeks. Trichrome staining confirms that the nanocomposite persists in the defects 4 weeks post-surgery (Figure 3I,O); however, by 8 weeks much of the nanocomposite has degraded (Figure 3U,AA). As expected, the nanocomposite material (without rhBMP-2) showed a significantly reduced bone volume fraction (Figure 3C), while both the rhBMP-2 groups showed higher BV/TV and bridging on histology. Bridging occurred in ≈80% of the defects in the rhBMP-2-nanocomposite mice, compared to 60% in the rhBMP-2-collagen sponge group, which often also shows a small area of fibrous tissue (Figure 3X, black arrow), indicating incomplete bridging.

2.4. Osterix mCherry Expression Correlates with Final Bone Mineral Content

Fluorescently tagged rhBMP-2 was tested in animals to determine the in vivo release kinetics of rhBMP-2 from either a collagen sponge or the nanocomposite. **Figure 4**A shows the fluorescent signal seen from the tagged rhBMP-2 in a calvarial defect model. The nanocomposite material shows a slower release with more rhBMP-2 retained especially early in the time course. In the collagen sponge group, much of the rhBMP-2 is released after 1 hr as indicated by the high fluorescence level,

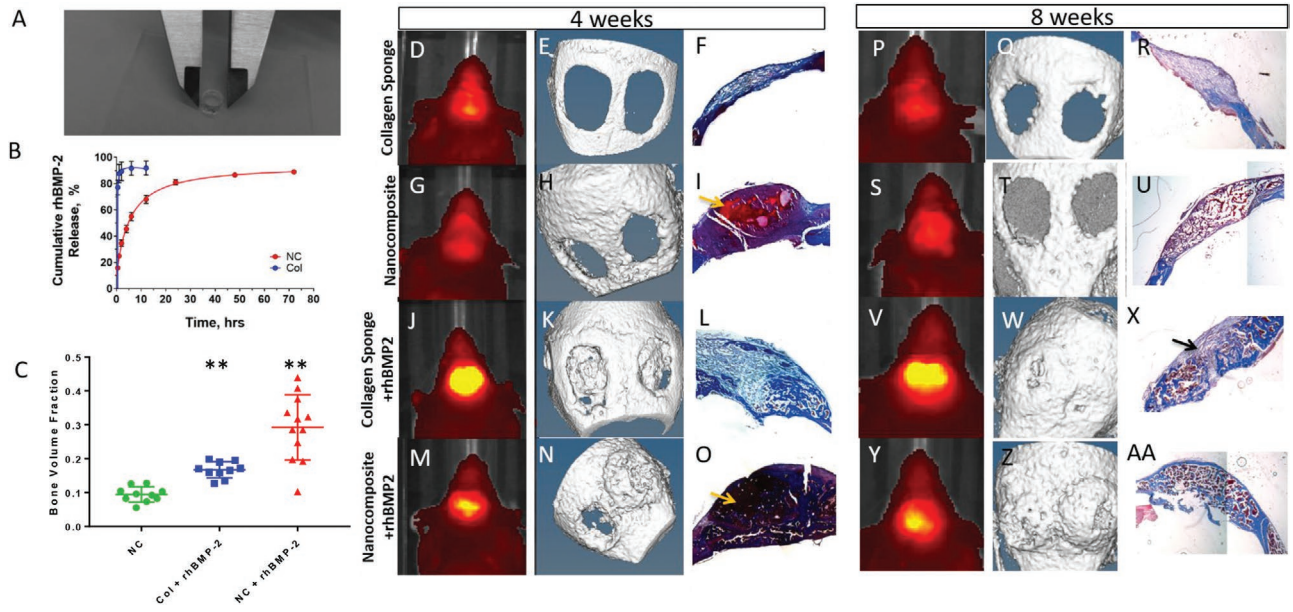

Figure 3. rhBMP-2-loaded material stimulates mineralization and bone volume fraction at 4 and 8 weeks. A) 6 mm nanocomposite hydrogel formed in a mold. B) Release of fluorescently tagged rhBMP-2 from nanocomposite (red, NC) or collagen sponge (blue, Col), $n = 3$. D,G,J,M,P,S,V,Y) IVIS imaging of a representative mouse. E,H,K,N,Q,T,W,Z) µCT imaging of a representative mouse. F,I,L,O,R,U,X,AA) Masson's Trichrome staining of a representative tissue section. Orange arrows show nanocomposite material in the defects. Black arrow indicates incomplete bridging, $n = 10$. C) Bone volume fraction (BV/TV) for treated groups (blue, collagen sponge with rhBMP-2; green, nanocomposite; red, nanocomposite with rhBMP-2), $n = 10$, $^{**}p < 0.05$.

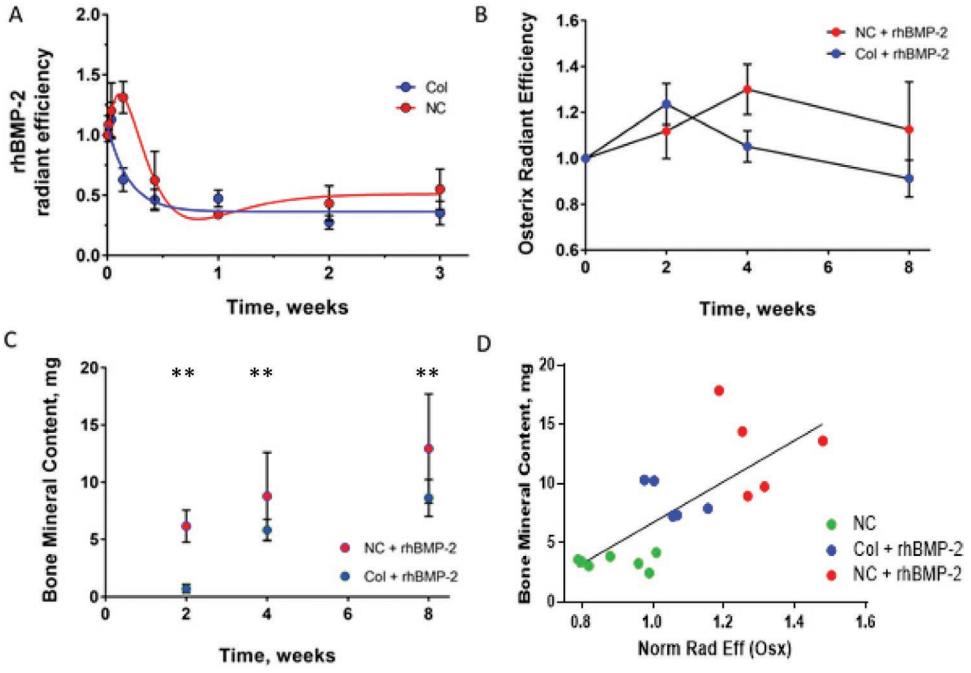

Figure 4. Osterix-mCherry expression correlates with final bone mineral content. A) Fluorescently labeled rhBMP-2 release in vivo showing an initial burst in both nanocomposite (red, NC) and collagen sponge (blue, Col) with prolonged release of rhBMP-2 in the nanocomposite group. B) Radiant efficiency of Osterix-mCherry as measured by IVIS over time post surgery (blue, collagen sponge with rhBMP-2; red, nanocomposite with rhBMP-2) indicating a response of these fluorescently labeled cells. C) Bone mineral content over time as measured via µCT (blue, collagen sponge with rhBMP-2; red, nanocomposite with rhBMP-2) showing equivalent bone formation in both groups. D) Correlation between final bone mineral content at 8 weeks and radiant efficiency as measured by IVIS at 4 weeks (blue, collagen sponge with rhBMP-2; green, nanocomposite; red, nanocomposite with rhBMP-2). For nanocomposite, $n = 6$, for all other groups $n = 5$. This is equivalent to 12 defects in the nanocomposite group and 10 defects in the other groups. $^{**}p < 0.05$.

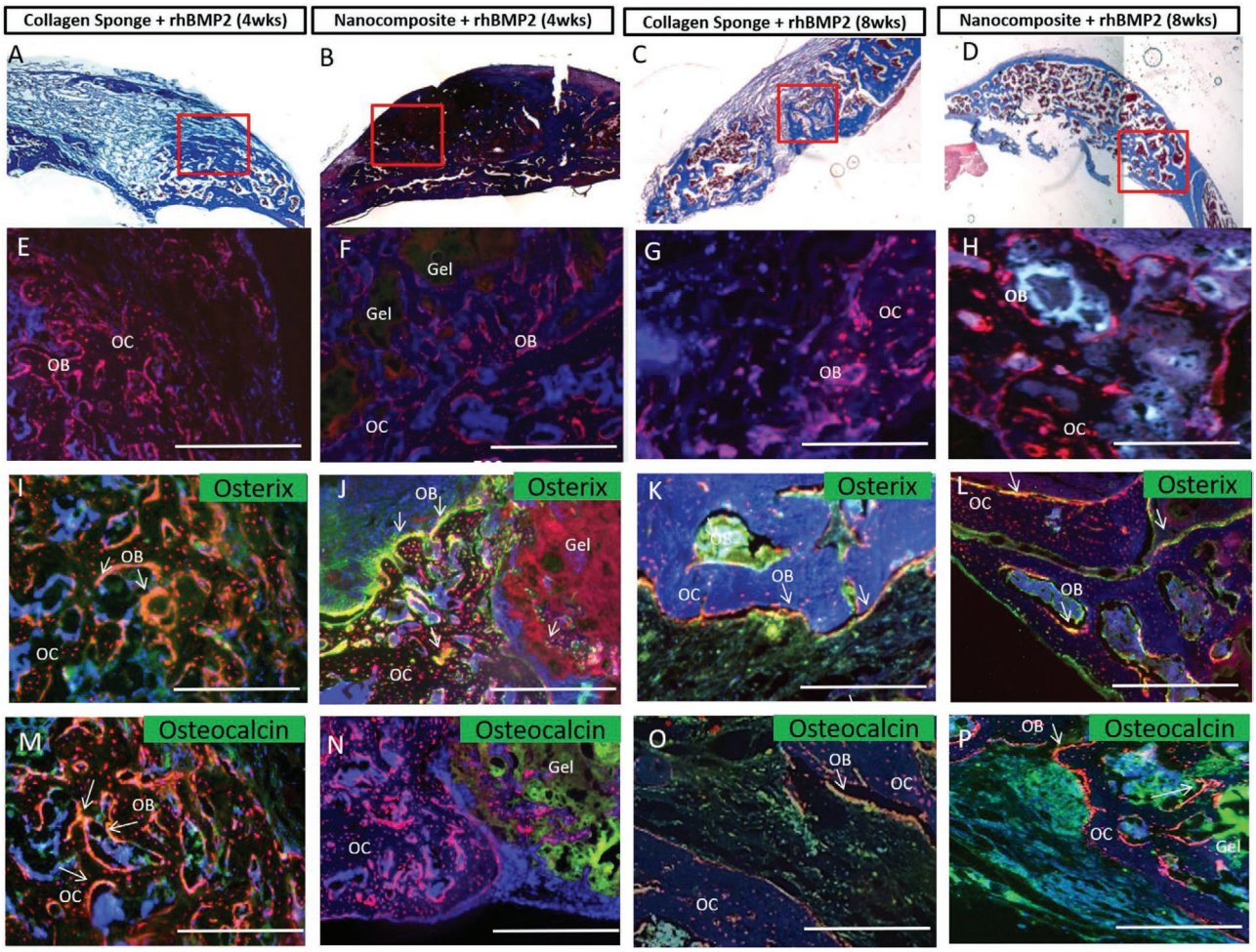

Figure 5. rhBMP-2-loaded materials stimulate Osterix and osteocalcin expression at 4 and 8 weeks. A) Collagen sponge treated with rhBMP-2 implanted for 4 weeks. B) Nanocomposite treated with rhBMP-2 implanted for 4 weeks. C) Collagen sponge treated with rhBMP-2 implanted for 8 weeks. D) Nanocomposite treated with rhBMP-2 implanted for 8 weeks. A–D) show Masson's Trichrome staining and the red boxes indicate the area of interest shown in subsequent sections. Collagen deposition stained in blue. E–H) images show endogenous Osterix expression as red fluorescence. DAPI is shown in blue. I–L) images show endogenous Osterix expression in red and immunostaining for Osterix in green. M–P) images show endogenous Osterix expression in red and areas of osteocalcin immunostaining in green. Overlap in all images is seen in yellow and marked with white arrows, marking the bone surface. The nanocomposite hydrogel has a distinct physical appearance and is marked. Scale bars = 500 mm. Gel, nanocomposite hydrogel; OB, osteoblasts; OC, osteocytes.

whereas the nanocomposite group shows its highest fluorescence intensity at 24 h. This is consistent with the burst release of rhBMP-2 seen by others.[47–50] Osterix-mCherry signal increased in the rhBMP-2-collagen sponge group until a peak at 2 weeks, followed by a decrease in signal until 8 weeks; in the rhBMP-2-nanocomposite group, the signal peaked at 4 weeks post-implantation (Figure 4B). This is statistically significant at 4 and 8 weeks. rhBMP-2 retention and Osterix-mCherry signal were correlated with mineralization by quantifying bone mineral content using μCT; bone content was higher in the rhBMP-2-nanocomposite group at 2, 4, and 8 weeks; both the collagen sponge and nanocomposite groups exhibited an increase in bone mineral content during defect repair (Figure 4C). This is statistically significant throughout the entire time course; p value < 0.05. At 4 weeks, the Osterix-mCherry signal from the rhBMP-2-collagen sponge and the rhBMP-2-nanocomposite groups are strongly correlative with final bone mineral content (Figure 4D), with a correlation coefficient of 0.74.

2.5. rhBMP-2-Loaded Materials Stimulate Osterix and Osteocalcin Expression at 4 and 8 Weeks

Osterix and Osteocalcin expression in regenerating bone tissues were confirmed through immunostaining at 4 and 8 weeks, with materials without rhBMP-2 acting as negative controls (Figure S2, Supporting Information). Using the Trichrome staining seen in Figure 3, we isolated a region at the edge of the original defect (**Figure 5**A–D, highlighted in red) for immunostaining. In tissues where rhBMP-2 was added, there is a robust cellular response at 4 and 8 weeks. Red cells, in the form of mesenchymal stem cells (MSC), osteoblasts (OB), and

osteocytes (OC) can be seen in the defect space (Figure 5E–H). Osterix expression was confirmed by immunostaining, which closely matched mCherry fluorescence (Figure 5I–L). At both 4 and 8 weeks, the bony edge of the Osterix-Cherry calvarium is clearly visible as red osteocytes embedded within the matrix and red osteoblasts on the bone surface. MSCs are also visible at early time points and can be identified by their location near, but not on, the bone surface within the marrow space or near the repairing defect. These cells can be differentiated from other bone cell types by their fibroblastic morphology. Osteoblasts can also be identified morphologically, as they are cuboidal and associated with the bone surface, often with a cobblestone-like appearance. Osteoblasts are also osteocalcin positive, due to the amount of mineral they excrete. Osteocytes are identified by their location within the bone tissue and by long processes extending from the cell body. All these bone cell types are red fluorescent. Cell identity was confirmed histologically.

Osteocalcin expression was also confirmed through immunostaining. Osteocalcin is secreted by osteoblasts, binds hydroxyapatite, plays a role in mineral nucleation, and serves as a direct marker of new bone formation and mineralization.[29,51,52] Osteocalcin is not observed in the nanocomposite only controls at either 4 or 8 week (Figure S2, Supporting Information). In rhBMP-2 treated defects, an increasing osteocalcin signal can be detected at 4 and 8 weeks (Figure 5M–P). This signal appears closest to where new bone is forming along the osteoblast surfaces and appears yellow due to the overlap with the Osterix-Cherry signal (see white arrows). Notably, the osteocalcin expression at 4 weeks in nanocomposite-treated defects was more modest than the expression in collagen sponges (Figure 5N), suggesting that new mineralization was more advanced in the collagen sponge condition at this time point despite the increased Osterix expression and 8 week mineral content in the nanocomposites.

3. Discussion

As researchers are working to develop therapeutics and delivery systems to induce bone formation, a need has arisen to find a way to test these therapeutics in vivo. Here, we demonstrate a facile method to predict late mineralization through the noninvasive tracking of biomarkers that herald bone repair. Currently, bone is assessed by the quantification of mineralization using μCT or X-ray, but it has become clear that the initiation of the bone formation process well precedes mineralization.

Healing of calvarial defects can rely on three potential reservoirs of progenitor cells in the periosteum, dura mater, and the cranial suture.[53–56] Each of these reservoirs stain positive for Osterix (Figure 1B,H) and were preserved by the surgical technique, which intentionally spared the dura, defect-adjacent periosteum, and suture. While IVIS imaging alone did not provide adequate resolution to determine the localization and source of Osterix-upregulated cells during defect repair, immunofluorescence and histology supported a repair process that began at the circumference of the defect (Figure 2G–I). This would suggest that the primary reservoir of progenitor cells to repair these defects was in the periosteum, as the dura mater was in contact with the entire defect area and the cranial suture was located medial to the defect.

During tissue repair, Osterix upregulation in progenitor cells and developing osteoblasts is an early indicator of bone formation. Typically, progenitor cells differentiate into osteoblasts which forms new bone, and these osteoblasts can become embedded in a matrix and ultimately differentiate into osteocytes.[57] Previous studies (Figure 1D) show that as these cells differentiate, the level of Osterix red fluorescence seen increases substantially, with osteocytes and osteoblasts showing the highest level of mCherry. We show here that high expression of Osterix is predictive of osteoblast formation and mineralization, and that this signal can be detected noninvasively using a fluorescent reporter. The increased Osterix-mCherry signal observed in rhBMP-2 treated defects (Figures 3J,M,V,Y and 4B) may be attributed to either increased per-cell Osterix expression or a substantial migration and proliferation of Osterix positive progenitor cells. It is likely that this is a combination of the two; certainly, the initially acellular defect is infiltrated by a large number of Osterix positive cells during defect repair; however, histological time courses showed much more robust and widely distributed Osterix-mCherry expression during healing at 4 weeks than at 8 weeks (Figures 2H,I and 5J,L), which correlated with IVIS signals (Figure 4B). Crucially, the control conditions implanted without rhBMP-2 showed substantial cell infiltration but no concomitant increase in Osterix expression or mineralization (Figure 3), supporting the role of rhBMP-2 in potentiating the recruitment and osteoblastic differentiation of progenitor cells in this model.

We tested our hypothesis that rhBMP-2-mediated mineralization could be predicted by early readouts of Osterix-mCherry signal using the clinical gold standard of an rhBMP-2-loaded collagen sponge, showing a strong correlation between Osterix-mCherry fluorescence and subsequent bone formation measured by μCT (Figure 4D). By comparison with a biomaterial exhibiting delayed rhBMP-2 release kinetics and increased in vivo retention, we were able to correlate rhBMP-2 presentation with temporal changes in Osterix expression and final bone mineral content. Although the underlying biomaterial systems were substantially different, rhBMP-2 negative controls of both materials showed poor endogenous healing, suggesting the materials were not themselves providing a confounding osteogenic signal. Of note, the fluorescence intensity (measured by radiant efficiency) seen in the nanocomposite reaches the same levels as those seen with rhBMP-2 on a collagen sponge, indicating this material is likely not impairing MSC infiltration or osteoblast differentiation. Temporal changes to Osterix expression were thus attributed to differences in rhBMP-2 presentation and release; these were in turn strongly correlated with final bone mineral content.

Sustained release of rhBMP-2, attained here when delivered from the nanocomposite, often results in a delayed but enhanced healing response.[49,50,58] This is likely due to the persistence of the growth factor causing an increase in its efficacy in vivo. rhBMP-2 burst release, from the collagen sponge, results in early stimulation of healing[49] (Figure 3B) with the high levels of Osterix-mCherry expression at 2 weeks; this early stimulation was evident in the higher osteocalcin deposition

noted in the collagen sponge at 4 weeks (Figure 5M). The enhancement in bone healing seen following sustained release of rhBMP-2 from the nanocomposite is likely due to enhanced activation and recruitment of progenitor cells,[5] as indicated by the increase in Osterix-mCherry signal up to 4 weeks, followed by a gradual decline, yet higher than that seen for the collagen group even through 8 weeks (Figure 4B, blue). This delayed Osterix upregulation was correlated with higher final bone mineral content and bone volume fraction (Figures 3C and 4C). Previous studies have shown that rhBMP-2 is crucial for the differentiation of mesenchymal stem cells into osteocytes[49] and that the longer the cells are exposed to rhBMP-2, the more osteoblastic traits they express.[3,52,59] Because the nanocomposite provides a depot of rhBMP-2, unlike the collagen sponge, we were able to visualize differences in bone repair between the two systems.

By tracking temporal expression of a marker that precedes mineralization, it is possible to use Osterix signal as a predictive model; though this is most strongly correlative after 4 weeks. Ultimately, it will likely be a mix of detection techniques during the first 4 weeks of bone repair which will provide the most complete picture of the developing repair tissue (μCT, immunohistochemistry, IVIS, etc.). Further study is needed to better understand the interplay between temporal presentation of osteogenic signals, cell infiltration and differentiation, and mineralization kinetics.

4. Conclusions

We developed a model system that allows for insight into the initial stages of bone repair, before definitive mineral deposition can be seen on either X-ray or μCT, using noninvasive fluorescence imaging. The Osterix-mCherry mouse model enables tracking recruited and differentiating MSCs before mineralization occurs and in the initial stages of bone repair. Quantification of bone formation at the molecular level allows us to gain insight into the interplay of progenitor cell recruitment and differentiation with mineralization. Osterix expression and eventual bone formation was dependent on rhBMP-2 release kinetics, in particular on the extent of sustained stimulation for recruitment and differentiation of MSCs into osteocytes, and hence can be used as a tool for the evaluation and optimization of osteogenic drug delivery platforms.

5. Experimental Section

Development of Dextran-Dendrimer Hydrogel Nanocomposite: A two-component material based on dextran aldehyde and generation-5 PAMAM dendrimer amine provided a cohesive hydrogel through aldehyde–amine cross-linking and an adhesive interface created by a dextran aldehyde-selective reaction with tissue amines. This hydrogel was augmented using two different aspect ratio nanoplatelets in our material. rhBMP-2 was added to the dextran such that the final concentration in the defect space was 0.2 μg.[46]

Animal Care and Maintenance: Osterix-mCherry mice were generously provided by the University of Connecticut. Transgenic animals were housed in a clean barrier facility and humanely treated in accordance with MIT institutional and IACUC guidelines.

Calvarial Defect Surgeries: 8–12 mice were used per experimental group. Mice were anesthetized with ketamine/xylazine and maintained on 0.5–1% isoflurane. Bilateral, full thickness, non-suture-associated critical sized calvarial defects were induced in 16-week-old Osterix-mCherry mice. A small incision (<1 cm) was be made in the skin above the midline of the skull. A 3.5–4 mm full thickness calvarial defect will be made with a diamond-coated trephine burr in the right and left parietal bone. The dura was left intact. Depending on the experimental group, defects were filled with an absorbable collagen sponge from an INFUSE bone graft kit (Medtronic), a PAMAM dendrimer/oxidized polysaccharide clay nanocomposite, collagen sponge infused with 0.2 μg rhBMP-2, or nanocomposite with 0.2 μg rhBMP-2. 3.5 mm diameter collagen sponges were created from a sheet of absorbable collagen sponge using a biopsy punch, while ≈20 μL of nanocomposite was injected into the calvarial defect and allowed to cure in situ. rhBMP-2 was obtained from INFUSE bone graft kits (Medtronic), labeled as described below, and reconstituted in either hydrogel macromer solutions or as directed by the manufacturer prior to application to collagen sponges. Wounds were closed with sutures. Mice were medicated every 12 h for the first 72 h with 0.1 mg kg^{-1} Buprenex for pain control.

MicroCT Imaging of Bone Growth: Mice were anesthetized with 1–2% isoflurane using a calibrated vaporizer inside an eXplore CT120 MicroCT (GE Healthcare) and noninvasively imaged for the extent and morphology of mineralization. Animals were imaged every 2 weeks, starting at week 2 and continuing for 8 weeks. Data was analyzed with Microview Software (Parallax Innovations, GE). A cylindrical region of interest 4 mm × 4 mm was created and aligned through the defect. Bone mineral content was measured using the Bone Analysis tool within the Parallax software suite. Auto-thresholding was set at 200 for all analyses performed.[60] Defects were classed as partially bridged if a single cross section showed continuous mineralized bone from one side of the defect to another. If all cross sections showed continuous mineralized bone, this was classed as fully bridged.

IVIS Imaging of Bone Growth: Mice were shaved then anesthetized with 1–2% isoflurane using a calibrated vaporizer inside an IVIS Spectrum (PerkinElmer). Images were taken with a 14 s exposure time. The excitation filter used was the 605 nm filter and the emission filter used was 660 nm to correlate with mCherry fluorescence. Images were obtained weekly, with the first set of images taken 1 day post-surgery to allow for recovery time for the mice.

For rhBMP-2 fluorescence, the exposure time was 0.5 s. The excitation filter used was 570 nm and the emission filter was 640 nm.

rhBMP-2 Release In Vitro and In Vivo: Nanocomposite discs loaded with 10 μg of fluorescently tagged rhBMP-2 (Alexa Fluor 594-NHS ester) were prepared from dextran and dendrimer solutions. In order to track rhBMP-2 release in vitro, the protein was tagged using the Alexa Fluor 594 succinimidyl ester (NHS ester) amine-reactive fluorophore. The protein and dye (1:5 molar ratio) were reacted in 0.1 M sodium bicarbonate buffer (pH = 8.3) for 1 h and protein-dye conjugate purified by extensive dialysis. Successful conjugation was confirmed by SDS-PAGE. The degradation rate of the materials was studied by conjugating fluorescent labels to both the dextran (Alexa Fluor 488 hydrazide) and dendrimer (Alexa Fluor 755 succinimidyl ester) components and following the release of these tagged polymers into PBS using a fluorescence microplate reader at 30 min, 1 h, 2 h, 6 h, 12 h, 24 h, and daily thereafter for up to 4 weeks. To avoid fluorescence quenching, <5% of fluorescently tagged materials was used in the final hydrogels. Degradation was also followed by mass loss measurement and results were correlated with loss of fluorescence method as previously published.[44] Subsequently, the nanocomposites were incubated in phosphate buffer saline (PBS, Gibco) at 37 °C. Release buffer (1 mL) was sampled at different time points ranging from 0.5 to 72 h. At each time point, 750 μL of the PBS was removed and replaced with fresh media. The release of rhBMP-2 protein was tracked by fluorescence signal at 585/617 for (excitation/emission) using a fluorimeter. Results were compared to a standard curve of known rhBMP-2 concentration in order to calculate the protein mass released. Each sample was performed in triplicate. Empty nanocomposite discs were used to analyze any

background fluorescent signal that may arise from the degradation of the materials over the experimental period.

Histological Preparation of Tissue Samples: Skulls were dissected and fixed in 10% formalin buffered in PBS for 7 days at 4 °C. Ten defects were acquired from the collagen sponge group, and 16 defects were acquired from all other groups. Tissues were decalcified in 0.1 N HCl, 0.25% glutaraldehyde in PBS for 7 days. Tissues were then placed in 30% sucrose overnight and finally embedded in Cryomedia (Thermo Scientific). Frozen 8 µm sections were obtained using a Leica Cryostat and Cryofilm type II tape transfer system (Section-Lab Co. Ltd.). Sequential tissue sections were mounted using 50% glycerol buffered in PBS for imaging.

Safranin O Staining: Sections were dried sections for 10 min, then hydrated with distilled water for 5 min. Sections were stained with Wiegert's iron hematoxylin working solution (Sigma) for 10 min. After staining, sections were washed in running tap water for 10 min, then stained with fast green solution (0.05% Fast Green, Sigma) for 5 min. Next sections were quickly rinsed with 1% acetic acid solution for no more than 10–15 s. Finally, sections were stained in 0.1% safranin O solution (Sigma) for 5 min. Sections were cleared with 95% ethyl alcohol for 2 min. Finally, sections were cover-slipped with a 50% glycerol, 50% PBS mixture.

Masson's Trichrome Staining: First sections were kept overnight in Bouin's Solution (Sigma), then rinsed in running tap water for 5–10 min to remove the yellow color. Next they were stained with Wiegert's iron hematoxylin working solution for 10 min followed by a rinse in tap water for 10 min. Sections were washed in distilled water, then stained in Biebrich scarlet-acid fuchsin solution for 10–15 min. After another wash in distilled water, sections were placed into a phosphomolybdic-phosphotungstic (1:1) acid solution for 10–15 min then transferred directly to aniline blue solution and stained for 5–10 min. Sections were rinsed briefly in distilled water and de-stained in a 1% acetic acid solution for 2–5 min. Finally, sections were washed in distilled water and dehydrated quickly through 95% ethyl alcohol. Sections were cover-slipped with a 50% glycerol, 50% PBS mixture.

DAPI Staining: 4′,6-Diamidino-2-phenylindole (DAPI) was diluted to 1:10 000 in PBS. Tissue sections were stained for 2–3 min in the dark then rinsed twice with PBS. Sections were cover-slipped with a 50% glycerol, 50% PBS mixture and imaged.

Microscopy and Imaging: Whole mount images of embryonic animals were taken using a Zeiss SteREO Lumar V.12 fluorescent microscope at 9.6× magnification using the Cherry (HQ577/20 Ex, HQ640/40 Em) filter set (Chroma Technologies) and photographed with an Axiocam MRm digital camera (Zeiss). Cultures were imaged on a Zeiss Observer Z.1 microscope using the Cherry (HQ577/20 Ex, HQ640/40 Em, Q595lp beam splitter) filter set (Chroma Technologies).

Tissues were imaged on a Nikon Ti-E fluorescent microscope using a Coolsnap EZ digital camera (Photometrics). Filters used were DAPI (EX340-380, DM400, BD435-485), FITC (EX465-495, DM505, BA551-555), TRITC (HYQ545/30, HYQ 620/60), and Cy5 (HYQ620/60 Ex, HYQ700/75 Em).

Immunostaining: Tissue sections were dried for 30 min at room temperature and then rehydrated by rinsing in PBS for 15 min. Aldehydes were quenched with 0.1% glycine for 5 min. Sections were then permeabilized for 30 min in 0.1% Triton X-100 (Sigma) at room temperature. Afterward, sections were washed twice for 10 min in PBS at room temperature. Nonspecific staining was blocked with a 1% BSA and 5% donkey or goat serum solution (Invitrogen) in PBS for 1 h. The blocking solution was removed, and the section was incubated in an Osterix rabbit polyclonal IgG primary antibody (Santa Cruz Biotechnologies A-13, sc-22536) at a 1:300 dilution or a was a rabbit polyclonal to osteocalcin (ab93876) at a 1:100 dilution in 1% BSA and 1% serum in PBS overnight at 4 °C. Tissue sections were then washed three times at 10 min per wash in PBS. Tissue sections were then suspended in a solution containing the secondary antibody, donkey anti-rabbit Alexa Fluor 488 (Invitrogen), or goat anti-rabbit Cy5 (Abcam) at a 1:100 dilution in 1% BSA and 1% donkey serum in PBS. Tissue sections were incubated with the secondary antibody at room temperature in the dark for 2 h. Sections were then washed three times for 10 min each in PBS and mounted on slides in 50% PBS-buffered glycerol for imaging.

Preparation of Bone Marrow Stromal Cells for Culture and FACS Sort: 3–4 week old Osterix-mCherry mice were sacrificed by CO_2 asphyxiation followed by cervical dislocation. Femurs and tibia were dissected. Bone marrow was collected through centrifugation. In brief, Eppendorf tubes, each containing a filter-less column, were prepared. 200 µL of sterile cold PFE (98%PBS, 2%FBS, 2 mM EDTA) were added to the bottom of the Eppendorf tube. Bones were spun at high speed for 3 min. Single cell suspensions were prepared by gently mixing the cells with a pipette followed by filtration through a 70-µm strainer. Cells which were to be analyzed immediately were subjected to a red blood cell lysis. For the red blood cell lysis, cells were pelleted and 1 mL of red blood cell lysing buffer (Sigma, R7757) was added to the pellet. This was gently mixed for 1 min then placed on ice for 3 min. The Red Blood Cell Lysing Buffer was diluted with 10 mL of PBS and then the cells were centrifuged at $350 \times g$ for 7 min. The supernatant was decanted, and the cells were prepared for further profiling.

Cells which were to be cultured did not undergo red blood cell lysis and were plated at a density of 1.2×10^6 cells cm^{-2} in DMEM culture medium containing 100 U mL^{-1} penicillin, 100 µg mL^{-1} streptomycin and 10% FCS (Hyclone). At day 4, the media was changed. In some cases, cells were cultured for a 21 day time period. In these cases, cells were grown in DMEM culture medium containing 100 U mL^{-1} penicillin, 100 µg mL^{-1} streptomycin, and 10% FCS (Hyclone) for 7 days, with the media being changed on Day 4 and Day 7. On Day 7, the media was switched to αMEM and supplemented with 50 µg mL^{-1} ascorbic acid and 8 mM 2-glycerol phosphate and changed every 2 days until Day 21.

FACS Analysis: Cultured cells were washed twice with cold PBS, then digested with a mixture of 0.1% Collagenase P (Roche), 0.1% Hyaluronidase (Sigma), 2% FBS (Hyclone), 49% OPTI-MEM (Gibco), and 49% PBS (Gibco). Cells were digested for 10 min at 37 °C, scraped, then digested for an additional 5 min. The digestion was stopped using an equal amount of media containing 2% FBS, 49% PBS, and 49% OPTI-MEM. Up to 10^7 nucleated cells were resuspended in 500 µL FACS staining buffer (PBS, 0.5% BSA, 2 mM EDTA, pH 7.2). Cells were analyzed on the FACS LSRII (BD) using the Red 649 nm Laser (670/30) and the YS 561 nm Laser (610/20, 600LP). The Blue 488 nm Laser (530/30, 505LP) was used to gate out auto-fluorescent cells.

Statistical Analysis: All statistical analysis was performed using GraphPad Prism. Results are represented as mean +/− standard error. No animals were excluded from the analysis. Sample sizes for Figures 3 and 4 is shown in the figure legend. One-way ANOVA was performed on the bone volume fraction measurements in Figure 3C. Linear and nonlinear regression analyses and Pearson correlation analyses were performed on IVIS and CT data sets in Figure 4A,B,D. Paired Student's *t*-tests were performed on the data sets from Figure 4C. Statistical significance was defined as p value <0.05.

Supporting Information

Supporting Information is available from the Wiley Online Library or from the author.

Acknowledgements

S.E.S., S.U., L.F.C., and N.A. designed the experiments. S.E.S., S.U., L.F.C., and D.P. performed experiments. S.E.S. and N.A. wrote the manuscript. S.E.S. and P.F.M. generated the Osterix-mCherry mice. E.R.E. and N.A. supervised the project. All authors discussed the results and reviewed the manuscript. E.R.E. was supported in part by a grant from NIH (R01 GM 49039) and some of the experiments by a

sponsored research agreement from Sanofi. The authors acknowledge the assistance of other members of the Edelman lab, the in vivo imaging core at MIT, and the Bio-Medical Engineering Department at Sanofi.

Conflict of Interest

The authors declare no conflict of interest.

Keywords

BMP-2, bone regeneration, imaging, nanocomposite, Osterix, scaffold

Received: August 14, 2019
Revised: September 11, 2019
Published online:

[1] L. Pimenta, L. Marchi, L. Oliveira, E. Coutinho, R. Amaral, *J. Neurol. Surg. A Cent. Eur. Neurosurg.* **2013**, *74*, 343.
[2] H. Nakahara, K. Takaoka, M. Koezuka, K. Sugamoto, T. Tsuda, K. Ono, *Clin. Orthop. Relat. Res.* **1989**, *239*, 299.
[3] B. H. Woo, B. F. Fink, R. Page, J. A. Schrier, Y. W. Jo, G. Jiang, M. DeLuca, H. C. Vasconez, P. P. DeLuca, *Pharm. Res.* **2001**, *18*, 1747.
[4] A. O. Mekhail, G. R. Bell, *Semin. Spine Surg.* **2008**, *20*, 257.
[5] J. D. Boerckel, Y. M. Kolambkar, K. M. Dupont, B. A. Uhrig, E. A. Phelps, H. Y. Stevens, A. J. García, R. E. Guldberg, *Biomaterials* **2011**, *32*, 5241.
[6] S. Khosla, J. J. Westendorf, M. J. Oursler, *J. Clin. Invest.* **2008**, *118*, 421.
[7] L. Oliveira, L. Marchi, E. Coutinho, N. Abdala, L. Pimenta, *World Spinal Column J.* **2010**, *1*, 19.
[8] R. Adams, S. Herrera-Nicol, A. Jenkins, *J. Neurol. Surg. Rep.* **2018**, *79*, e70.
[9] P. N. Bodalia, V. Balaji, R. Kaila, L. Wilson, *Bone Joint Res.* **2016**, *5*, 145.
[10] V. Joseph, Y. R. Rampersaud, *Spine* **2007**, *32*, 2885.
[11] D. M. R. Gibbs, C. R. M. Black, G. Hulsart-Billstrom, P. Shi, E. Scarpa, R. O. C. Oreffo, J. I. Dawson, *Biomaterials* **2016**, *99*, 16.
[12] H. Inoda, G. Yamamoto, T. Hattori, *Int. J. Oral Surg.* **2007**, *36*, 39.
[13] A. A. Sawyer, S. J. Song, E. Susanto, P. Chuan, C. X. F. Lam, M. A. Woodruff, D. W. Hutmacher, S. M. Cool, *Biomaterials* **2009**, *30*, 2479.
[14] P. D. Mariner, J. M. Wudel, D. E. Miller, E. E. Genova, S. O. Streubel, K. S. Anseth, *J. Orthop. Res.* **2013**, *31*, 401.
[15] S. E. Lobo, T. L. Arinzeh, *Materials* **2010**, *3*, 815.
[16] F. A. Müller, L. Müller, I. Hofmann, P. Greil, M. M. Wenzel, R. Staudenmaier, *Biomaterials* **2006**, *27*, 3955.
[17] H. D. Kim, S. Amirthalingam, S. L. Kim, S. S. Lee, J. Rangasamy, N. S. Hwang, *Adv. Healthcare Mater.* **2017**, *6*, 1700612. https://doi.org/10.1002/adhm.201700612
[18] C. Szpalski, M. Wetterau, J. Barr, S. M. Warren, *Tissue Eng., Part B* **2011**, *18*, 246.
[19] G. Rucher, L. Cameliere, J. Fendri, A. Abbas, K. Dupont, S. Kamel, N. Delcroix, A. Dupont, L. Berger, A. Manrique, *Mol. Imaging Biol.* **2018**, *20*, 984.
[20] A.-M. Collignon, J. Lesieur, N. Anizan, R. B. Azzouna, A. Poliard, C. Gorin, D. Letourneur, C. Chaussain, F. Rouzet, G. Y. Rochefort, *Acta Biomater.* **2018**, *82*, 111.
[21] Z. A. Zhong, A. Peck, S. Li, J. VanOss, J. Snider, C. J. Droscha, T. A. Chang, B. O. Williams, *Bone Res.* **2015**, *3*, 15013.
[22] P. S. Lienemann, S. Metzger, A. S. Kiveliö, A. Blanc, P. Papageorgiou, A. Astolfo, B. R. Pinzer, P. Cinelli, F. E. Weber, R. Schibli, M. Béhé, M. Ehrbar, *Sci. Rep.* **2015**, *5*, 10238.
[23] M. Ventura, G. M. Franssen, E. Oosterwijk, O. C. Boerman, J. A. Jansen, X. F. Walboomers, *J. Tissue Eng. Regener. Med.* **2016**, *10*, 843.
[24] K. Vintersten, C. Monetti, M. Gertsenstein, P. Zhang, L. Laszlo, S. Biechele, A. Nagy, *Genesis* **2004**, *40*, 241.
[25] D. C. Prasher, *Trends Genet.* **1995**, *11*, 320.
[26] D. Fink, S. Wohrer, M. Pfeffer, T. Tombe, C. J. Ong, P. H. B. Sorensen, *Genesis* **2010**, *48*, 723.
[27] Y. Liu, S. Strecker, L. Wang, M. S. Kronenberg, W. Wang, D. W. Rowe, P. Maye, *PLoS One* **2013**, *8*, e71318.
[28] L. E. Kaback, D. Y. Soung, A. Naik, N. Smith, E. M. Schwarz, R. J. O'Keefe, H. Drissi, *J. Cell. Physiol.* **2008**, *214*, 173.
[29] T. Matsubara, K. Kida, A. Yamaguchi, K. Hata, F. Ichida, H. Meguro, H. Aburatani, R. Nishimura, T. Yoneda, *J. Biol. Chem.* **2008**, *283*, 29119.
[30] H. Rashid, C. Ma, H. Chen, H. Wang, M. Q. Hassan, K. Sinha, B. de Crombrugghe, A. Javed, *Connect. Tissue Res.* **2014**, *55*, 83.
[31] L. A. Kaback, Y. Soung do, A. Naik, N. Smith, E. M. Schwarz, R. J. O'Keefe, H. Drissi, *J. Cell. Physiol.* **2008**, *214*, 173.
[32] M. Hatta, Y. Yoshimura, Y. Deyama, A. Fukamizu, K. Suzuki, *Int. J. Mol Med.* **2006**, *17*, 425.
[33] K. Nakashima, X. Zhou, G. Kunkel, Z. Zhang, J. M. Deng, R. R. Behringer, B. De Crombrugghe, *Cell* **2002**, *108*, 17.
[34] J. Renn, C. Winkler, *Dev. Dyn.* **2009**, *238*, 241.
[35] M. Milona, J. E. Gough, A. J. Edgar, *BMC Genomics* **2003**, *4*, 43.
[36] S. Strecker, Y. Fu, Y. Liu, P. Maye, *Genesis* **2013**, *51*, 246.
[37] D. B. Burr, O. Akkus, in *Basic and Applied Bone Biology*, Academic Press, London, UK **2013**, pp. 3–25.
[38] H. Nakamura, *J. Hard Tissue Biol.* **2007**, *16*, 15.
[39] J. J. Montesinos, E. Flores-Figueroa, S. Castillo-Medina, P. Flores-Guzmán, E. Hernández-Estévez, G. Fajardo-Orduña, S. Orozco, H. Mayani, *Cytotherapy* **2009**, *11*, 163.
[40] K. Irie, S. Ejiri, Y. Sakakura, T. Shibui, T. Yajima, *J. Histochem. Cytochem.* **2008**, *56*, 561.
[41] P. S. Gomes, M. H. Fernandes, *Lab. Anim.* **2011**, *45*, 14.
[42] D. E. Lieberman, O. M. Pearson, J. D. Polk, B. Demes, *J. Exp. Biol.* **2003**, *206*, 3125.
[43] N. Artzi, N. Oliva, C. Puron, S. Shitreet, S. Artzi, A. bon Ramos, A. Groothuis, G. Sahagian, E. R. Edelman, *Nat. Mater.* **2011**, *10*, 704.
[44] N. Artzi, T. Shazly, A. B. Baker, A. Bon, E. R. Edelman, *Adv. Mater.* **2009**, *21*, 3399.
[45] P. K. Shrivastava, R. Singh, S. K. Shrivastava, *Chem. Pap.* **2010**, *64*, 592.
[46] S. Unterman, L. F. Charles, S. E. Strecker, D. Kramarenko, D. Pivovarchik, E. R. Edelman, N. Artzi, *ACS Nano* **2017**, *11*, 2598.
[47] A. Sharma, F. Meyer, M. Hyvonen, S. M. Best, R. E. Cameron, N. Rushton, *Bone Joint Res.* **2012**, *1*, 145.
[48] S. Suliman, Z. Xing, X. Wu, Y. Xue, T. O. Pedersen, Y. Sun, A. P. Døskeland, J. Nickel, T. Waag, H. Lygre, A. Finne-Wistrand, D. Steinmüller-Nethl, A. Krueger, K. Mustafa, *J. Controlled Release* **2015**, *197*, 148.
[49] M. Faßbender, S. Minkwitz, C. Strobel, G. Schmidmaier, B. Wildemann, *Int. J. Mol. Sci.* **2014**, *15*, 8539.
[50] J. J. Patel, C. L. Flanagan, S. J. Hollister, *Tissue Eng., Part C* **2014**, *21*, 489.
[51] S. Srouji, E. Livne, *Mech. Ageing Dev.* **2005**, *126*, 281.
[52] D. A. Puleo, W. W. Huh, S. S. Duggirala, P. P. DeLuca, *J. Biomed. Mater. Res.* **1998**, *41*, 104.
[53] F. Crisera, S. Warren, J. Greenwald, J. Spector, Z. Peled, P. Bouletreau, M. Longaker, in *Craniofacial Surgery*, Vol. 9, Editografica s.r.l., Bologna, Italy **2001**.

[54] Y. C. Por, C. R. Barcel??, K. E. Salyer, D. G. Genecov, K. Troxel, E. Gendler, M. E. Elsalanty, L. A. Opperman, *Ann. Acad. Med. Singapore* **2007**, *36*, 911.
[55] S. M. Warren, J. A. Greenwald, R. P. Nacamuli, K. D. Fong, H. J. M. Song, T. D. Fang, J. A. Mathy, M. T. Longaker, *J. Craniofac. Surg.* **2003**, *14*, 363.
[56] R. C. Ogle, S. S. Tholpady, K. A. McGlynn, R. A. Ogle, *Cells Tissues Organs* **2004**, *176*, 54.
[57] C. S. Soltanoff, S. Yang, W. Chen, Y.-P. Li, *Crit. Rev. Eukaryotic Gene Expression* **2009**, *19*, 1.
[58] R. Reyes, J. A. Rodríguez, J. Orbe, M. R. Arnau, C. Évora, A. Delgado, *Drug Delivery* **2018**, *25*, 750.
[59] D. A. Puleo, *J. Cell. Physiol.* **1997**, *173*, 93.
[60] K. Verdelis, L. Lukashova, E. Atti, P. Mayer-Kuckuk, M. G. E. Peterson, S. Tetradis, A. L. Boskey, M. C. H. van der Meulen, *Bone* **2011**, *49*, 580.

